Designing dual-center redox-active π-systems with ultra-low gap for enhanced capacitive deionization desalination

Hao Zhou[a], *Jun Yang*[a,*], *Yuxi Huang*[a], *Kouhua Li*[a], *Chuanyan Li*[a], *Minjie Shi*[a] *and Edison Huixiang Ang*[b,*]

[a]School of Materials Science and Engineering, Jiangsu University of Science and Technology, Jiangsu 212003, P. R. China. E-mail addresses: iamjyang@just.edu.cn

[b]Natural Sciences and Science Education, National Institute of Education, Nanyang Technological University, Singapore 637616, Singapore. E-mail address: edison.ang@nie.edu.sg (E. H. Ang)

Experimental section

Material preparation

All reagents were purchased from Aladdin and used directly without further purification. First, 0.26818 g of 1,4,5,8-naphthalenetetracarboxylic dianhydride (NTCDA) and 0.1582 g of 2,3-diaminonaphthalene (2,3-DAN) were added to 20 mL of N,N-dimethylformamide (DMF) and ultrasonically mixed. The resulting solution was then transferred into a reaction kettle and heated at 200 °C for 12 h. After cooling to room temperature, the obtained mixture was centrifuged, washed repeatedly with DMF, ethanol, and water, and dried to yield a black powder. The yield of PIND was approximately 40–50%

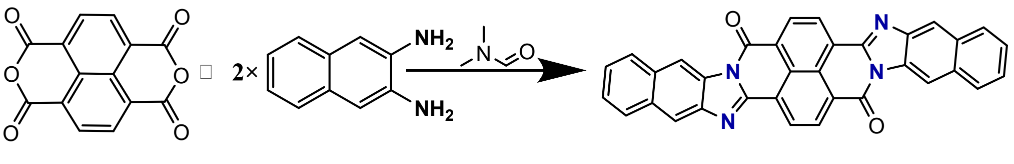

Figure S1. Schematic illustration for the synthetic route of PIND.

Characterization methods

The morphology and microstructure of the synthesized PIND polymer were analyzed using multiple characterization techniques. The surface morphology was examined by scanning electron microscopy (SEM; FEI Nova NanoSem450), and the structural features were identified by nuclear magnetic resonance spectroscopy (NMR; Bruker Avance III, 400 MHz). The microstructural morphology was further investigated using transmission electron microscopy (TEM; Tecnai G220S-Twin), while functional groups were determined via Fourier-transform infrared spectroscopy (FT-IR; Thermo Fisher Scientific Nicolet 6700). The crystalline structure was characterized by X-ray diffraction (XRD; Bruker D8, equipped with a 2D detector, Cu Kα, $\lambda = 1.54$ Å), and elemental composition as well as chemical states were analyzed by X-ray photoelectron spectroscopy (XPS; Thermo Fisher K-Alpha). UV-visible absorption spectroscopy (UV-Vis) measurements were obtained using a Hitachi U-4100 spectrophotometer. For the in-situ UV test, Ag/AgCl served as the reference electrode, platinum wire as the counter electrode, and 1 M NaCl was used as the electrolyte in the in-situ reaction tank.

All theoretical calculations were performed using the density functional theory (DFT) method implemented in the commercial Gaussian 16 software package. The geometries of the studied organic material and its Na-ion complexes were fully optimized at the B3LYP-D3/6-311G(d) level of theory, and vibrational frequency analyses were carried out at the same level. The localized orbital locator (LOL-π), reduced density gradient (RDG), harmonic oscillator model of aromaticity (HOMA), and molecular electrostatic potential (MESP) wave function cubes were calculated using the Multiwfn 3.8 (dev) code and visualized with the VMD software.

Electrochemical measurements

PIND, acetylene black, and polyvinylidene fluoride (PVDF) were mixed in N-methy l-2-pyrrolidone (NMP) solution at a mass ratio of 7:2:1 and stirred for 12 hours to obtain homogeneous slurry. The resulting slurry was uniformly coated onto graphite paper and dried overnight in a vacuum oven at 60 °C, with an active material loading of 1.2 mg cm^{-2}.

Electrochemical measurements were conducted in 0.5 M NaCl aqueous solution using an electrochemical workstation (DH7000C, Donghua) in a three-electrode configuration, where the prepared PIND electrode, a graphite rod, and a saturated Ag/AgCl electrode served as the working, counter, and reference electrodes, respectively. The specific capacitance (C, F g^{-1}) was calculated from the galvanostatic charge–discharge (GCD) curves according to the following equation S1.

$$C = \frac{I\Delta t}{m\Delta V} \tag{S1}$$

where I (A), Δt (s), ΔV (V) and m (g) correspond to discharging current, discharging time, potential window, and active mass of the PPWHA electrode, respectively. EIS tests were implemented in the frequency range of 100 kHz to 0.01 Hz. The Na^+ diffusion process within the electrode can be qualitatively calculated by diffusion coefficient (D, cm^2 s^{-1}) according to Equation S2 and S3:

$$D = \frac{R^2T^2}{2A^2n^4F^4C^2\sigma^2} \tag{S2}$$

$$Z' = \sigma\omega^{-1/2} \tag{S3}$$

where R, T, A, n, F, and C refer to gas constant (8.314 J K^{-1} mol^{-1}), absolute temperature (298 K), electrode surface area (cm^2), number of transferred electrons, Faraday constant, and Na^+ concentration, respectively. Z' and σ are the real part impedance and Warburg factor, respectively.

Desalination experiments

The electrosorption tests were measured by an HCDI device by using PIND polymer as anode and commercial AC as cathode, with an anion exchange membrane placed near the AC cathode to prevent cation capture during voltage reversal, while the total mass loading of active materials on anode and cathode was about 50 mg. Saline water (500 mg L^{-1}) was pumped into the constructed HCDI device through a peristaltic pump at a fixed flow rate of 10 mL min^{-1}. The real-time conductivity of saline water was monitored by an online conductivity meter (DDSJ-308F), and the concentration of saline water was calculated based on the calibration curve between the concentration and conductivity. The salt removal was carried out at different imposed voltages (0.8, 1.0, 1.2, and 1.4 V) for 0.5 h, and the corresponding desorption was operated at the reverse voltage for the same time.

The desalination performance of the constructed HCDI device was evaluated by salt adsorption capacity (SAC, mg g^{-1}), average salt adsorption rate ($ASAR$, mg g^{-1} min^{-1}), charge efficiency (Λ), and energy consumption (E, Wh g^{-1}) with the following Equation S4-S7:

$$SAC=\frac{(C_0-C_e)\times V\times K}{m} \quad \text{(S4)}$$

$$ASAR=\frac{SAC}{t} \quad \text{(S5)}$$

$$\Lambda=\frac{m\times SAC\times F}{M\times\int Idt}\times 100\% \quad \text{(S6)}$$

$$E=\frac{U\times\int Idt}{3.6\times(C_e-C_0)\times V} \quad \text{(S7)}$$

where C_0 and C_e (mg L^{-1}) are concentrations of influent and effluent saline water; V (L), m (g) and t (s) refer to the volume of saline solution, total mass of two electrodes, K= molar mass of the ion / molar mass of the solute and the adsorption time, respectively; F (96485 C mol^{-1}), M (58.5 g mol^{-1}), I (A) and U (V) correspond to Faraday constant, molar mass of NaCl, transient current at the adsorption time, and applied voltage, respectively.

The nonlinear equations of pseudo-first-order (**Eq. S8**) and pseudo-second-order models (**Eq. S9**) were used to investigate the adsorption kinetic data of the constructed HCDI device.

$$Q_t=Q_e\left(1-exp^{-K_1t}\right) \quad \text{(S8)}$$

$$Q_t=\frac{K_2{Q_e}^2t}{1+K_2Q_et} \quad \text{(S9)}$$

where Q_t (mg g^{-1}) is instant adsorption quantity at time, t (min) and Q_e (mg g^{-1}) are adsorption time and equilibrium adsorption capacity. k_1 (min^{-1}) and k_2 (g mg^{-1} min^{-1}) correspond to rate constants of pseudo-first-order and pseudo-second-order, respectively.

Theoretical calculation

All calculations were performed using the Density Functional Theory (DFT) method, as implemented in the commercial Gaussian 16 software package (Gaussian, Inc.). The molecular structures of PIND and its monomers were optimized at the B3LYP/def2-SVP level of theory. This combination of method, functional, and software was employed to derive both the optimized geometries and the corresponding vibrational frequencies of the compounds under investigation. Additionally, the geometry of PIND was optimized to ensure the lowest total energy configuration. Localized Orbital Locator-π (LOL-π), Reduced Density Gradient (RDG), Harmonic Oscillator Model of Aromaticity (HOMA), Adsorption energy, Differential charge and Molecular Electrostatic Potential (MESP) wave function cubes were computed using the Multiwfn 3.8 (dev) code, with visualization carried out using VMD software. The electrostatic potential (ESP) was derived by solving the Poisson equation for the charge distribution and mapping it onto the molecular surface. The color-coded ESP maps reflect electron density distribution, where red indicates electron-rich regions (negative ESP), and blue represents electron-deficient regions (positive ESP). The transformation of molecular structures from PIND to PIND + $2Na^+$ and PIND + $4Na^+$ follows a stepwise reduction process. The energy changes were evaluated via the Gibbs free energy change (ΔG) for each step, with the reaction potential expressed by the equation $E = -\Delta G/nF$, where n denotes the number of transferred electrons and F is the Faraday constant.

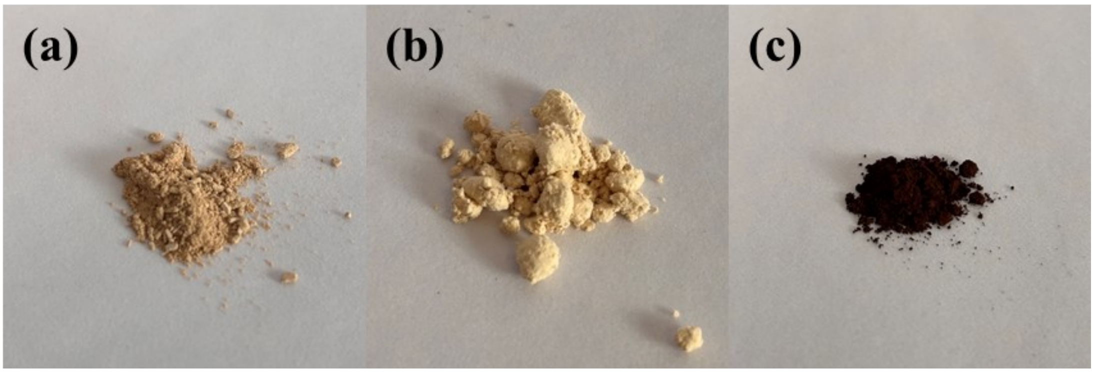

Fig. S2. Digital photos of (a) DAN, (b) NTCDA precursors, and (d) PIND molecule.

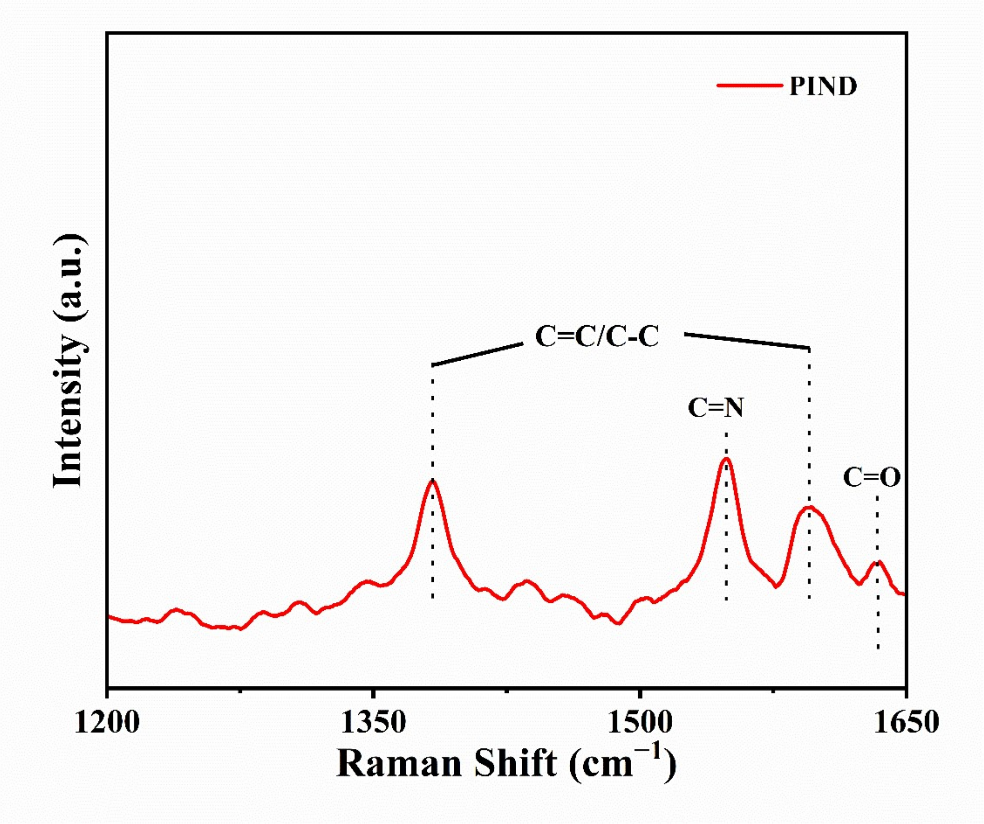

Fig S3. Raman spectrum of PIND electrode.

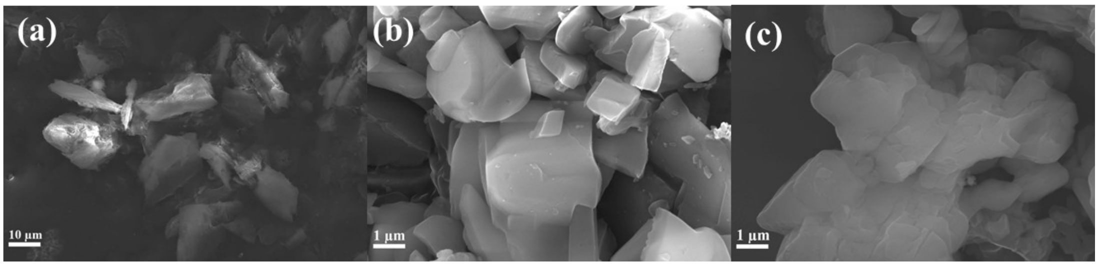

Fig. S4. SEM images of (a) DAN, (b) NTCDA precursors, and (c) PIND molecule.

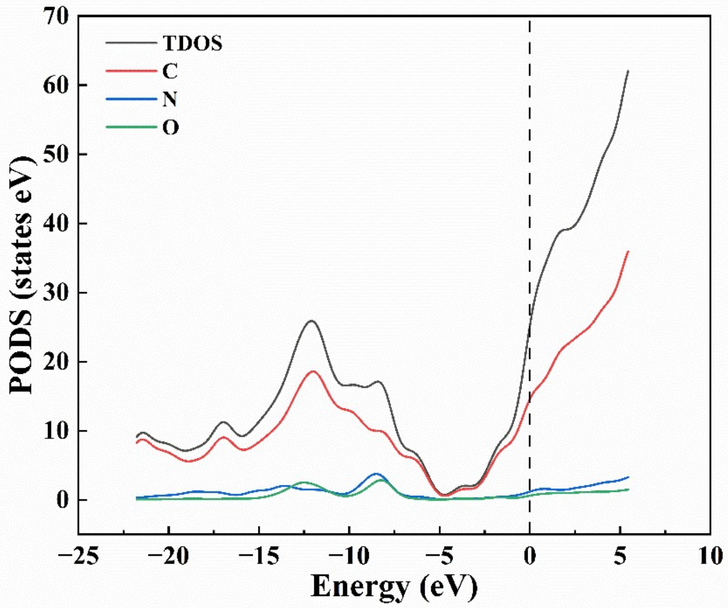

Fig. S5. PDOS pattern of the PIND molecule.

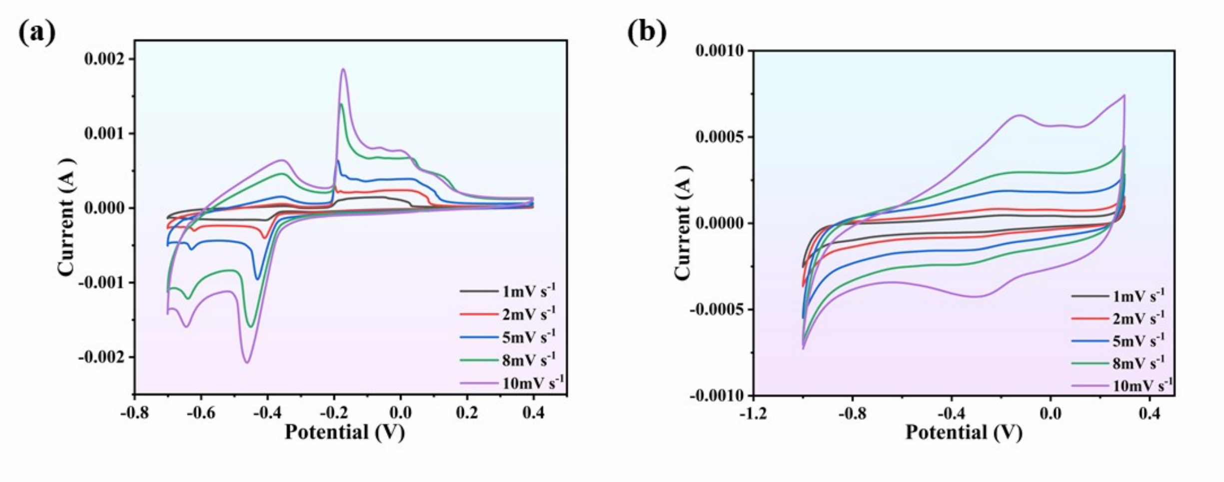

Fig S6. CV curves of (a) NTCDA and (b) DAN under different scan rates.

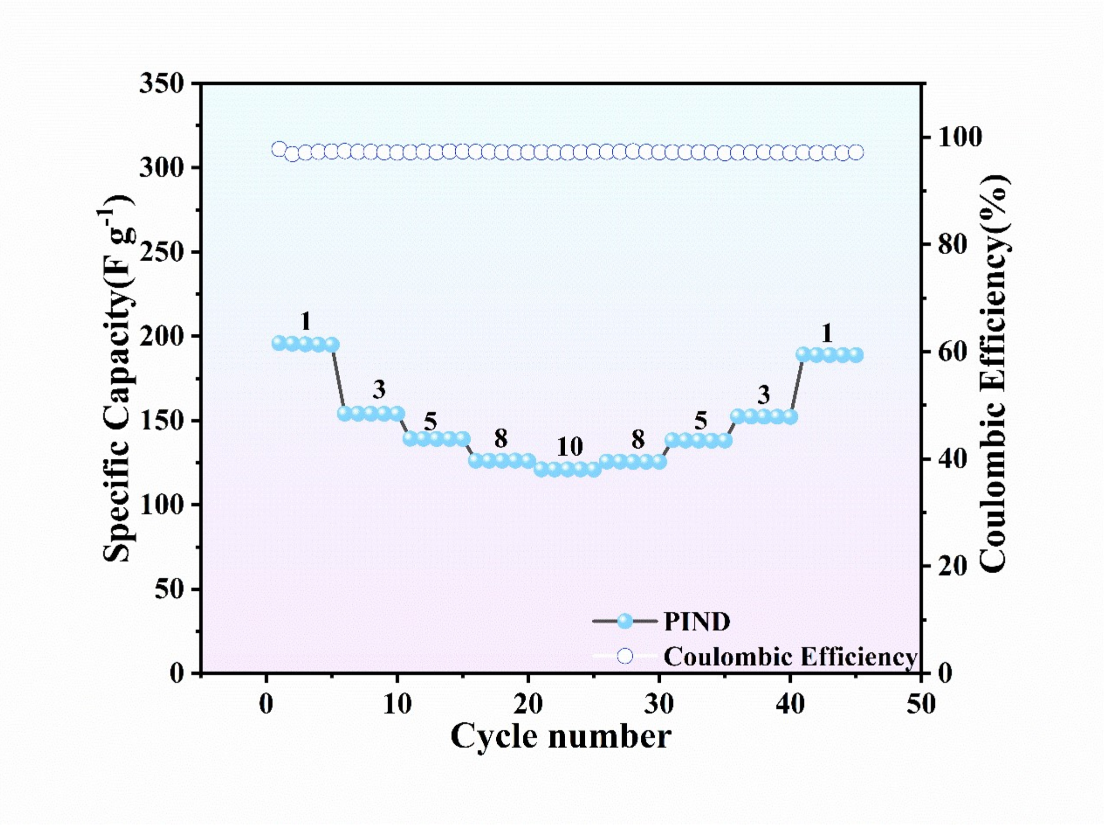

Fig S7. Rate performance of PIND.

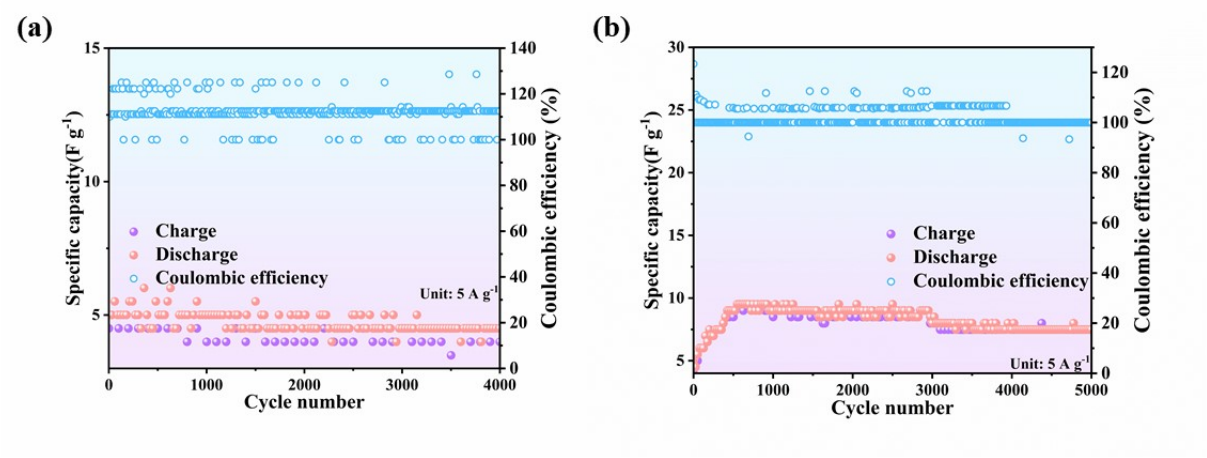

Fig S8. Long term cycle stability of (a) NTCDA and (b) DAN at 5 A g^{-1} current density.

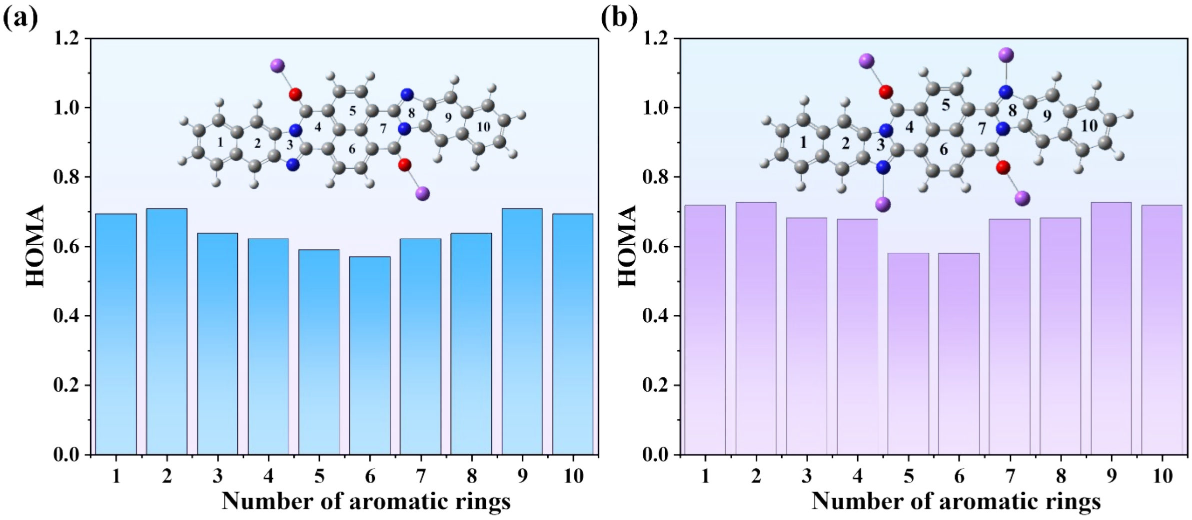

Fig S9. HOMA of (a) PIND +2Na and (b) PIND +4Na.

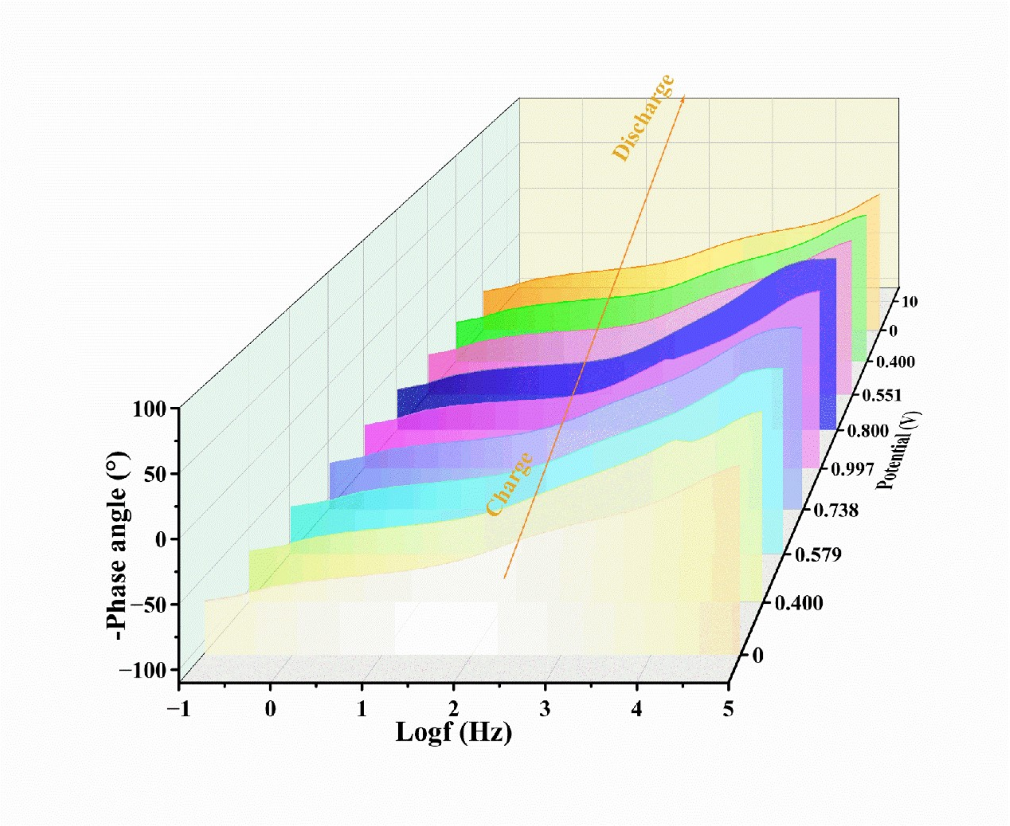

Fig S10. Bode plots of the PIND electrode at different charge/discharge states.

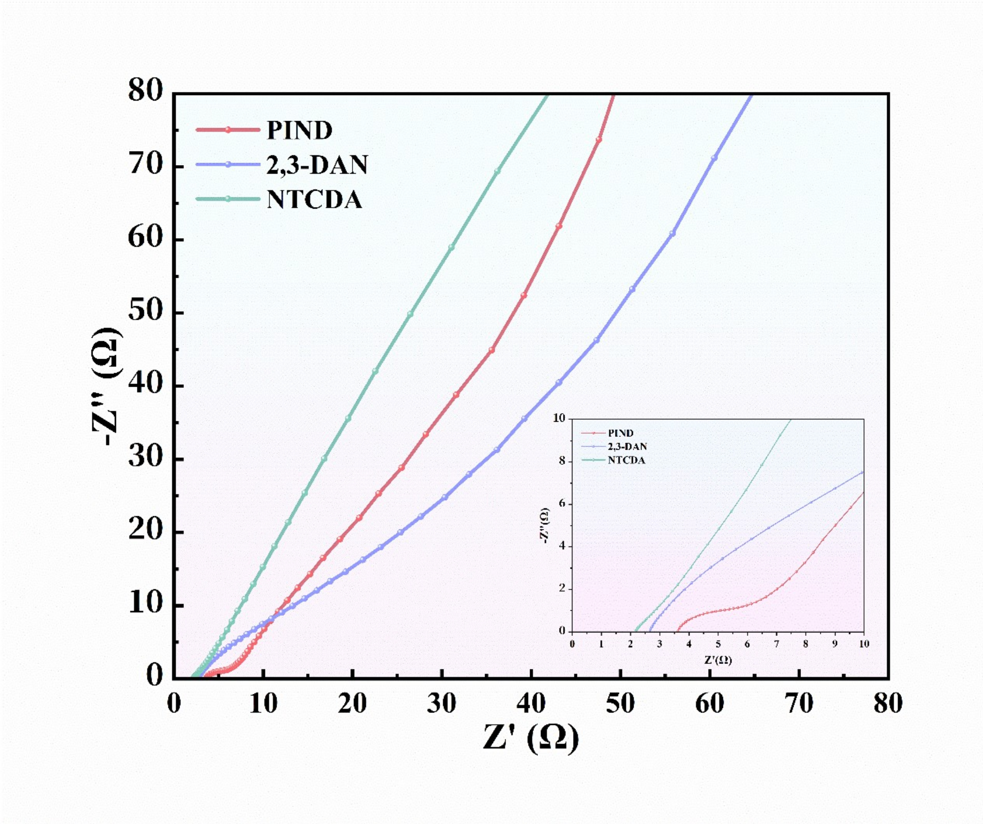

Fig S11. Nyquist of PIND, DAN, and NTCDA.

Tab.S1. The obtained equivalent series resistance (R_s), charge transfer resistance (R_{ct}) and Warburg impedance (Z_w) of the PIND, NTCDA, and DAN electrode

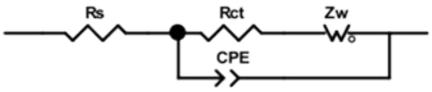	R_s (Ω)	R_{ct} (Ω)	Z_w (Ω)
PIND	**3.58**	**2.84**	**5.70**
NTCDA	**3.30**	**5.69**	**8.76**
2,3-DAN	**2.59**	**45.97**	**62.56**

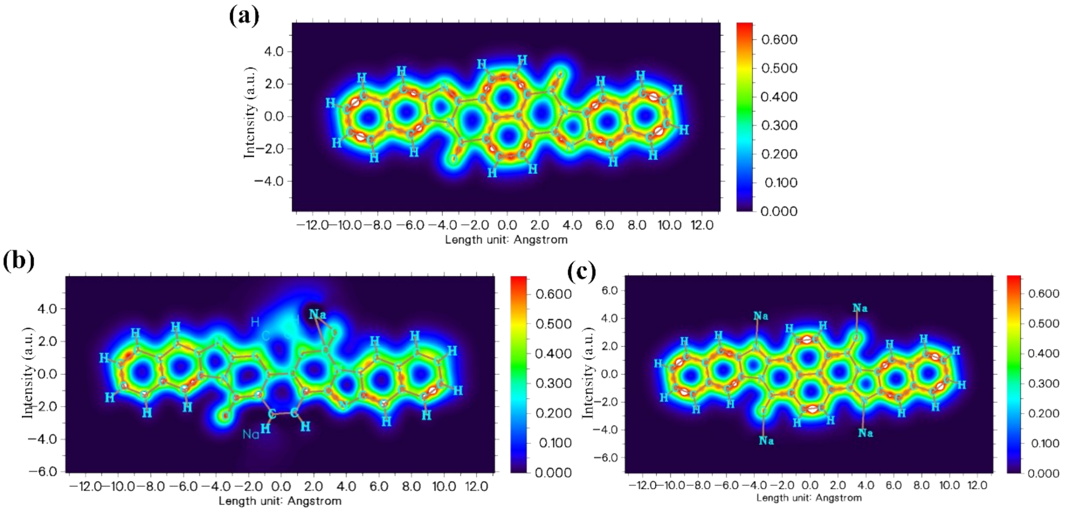

Fig S12. localized orbital locator-π diagram of the (a) PIND, (b) PIND+2Na, and (c)PIND+4Na.

Tab. S2. Distribution of electrostatic potential values at different redox active sites in the PIND molecule.

Redox active sites	**Atom**	**Electrostatic Potential (kcal mol^{-1})**
Site A	**N**	**-24.42036**
Site B	**O**	**-27.299144**
Site C	**O**	**-27.304385**
Site D	**N**	**-24.428540**

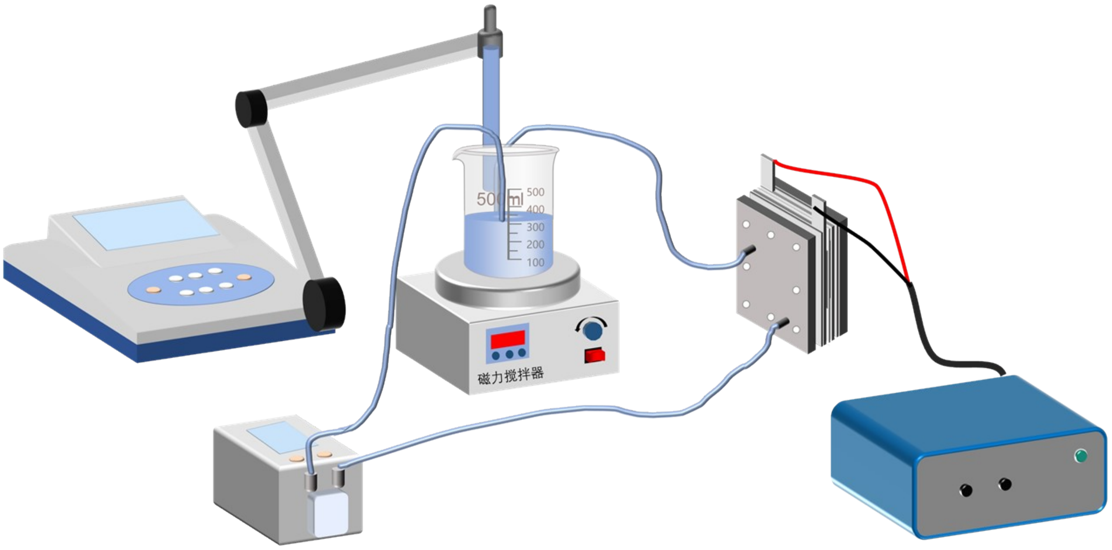

Fig S13. Schematic diagram of the constructed PIND||AC HCDI system.

To ensure reproducibility and clarity of the CDI measurements, detailed experimental procedures are provided in **Fig. S13.** Briefly, hybrid capacitive deionization (HCDI) tests were conducted in a two-electrode cell using PIND as the cation-capture electrode and activated carbon (AC) as the counter electrode, separated by an ion-exchange membrane. An aqueous NaCl solution was used as a model brackish feed and operated in batch mode. A constant cell voltage of 1.4 V was applied for 30 min for electrosorption, followed by polarity reversal for regeneration. The salt concentration was monitored by conductivity and converted to NaCl concentration using a pre-calibrated conductivity–concentration curve. All salt adsorption metrics were calculated based on NaCl concentration changes and normalized to the mass of PIND.

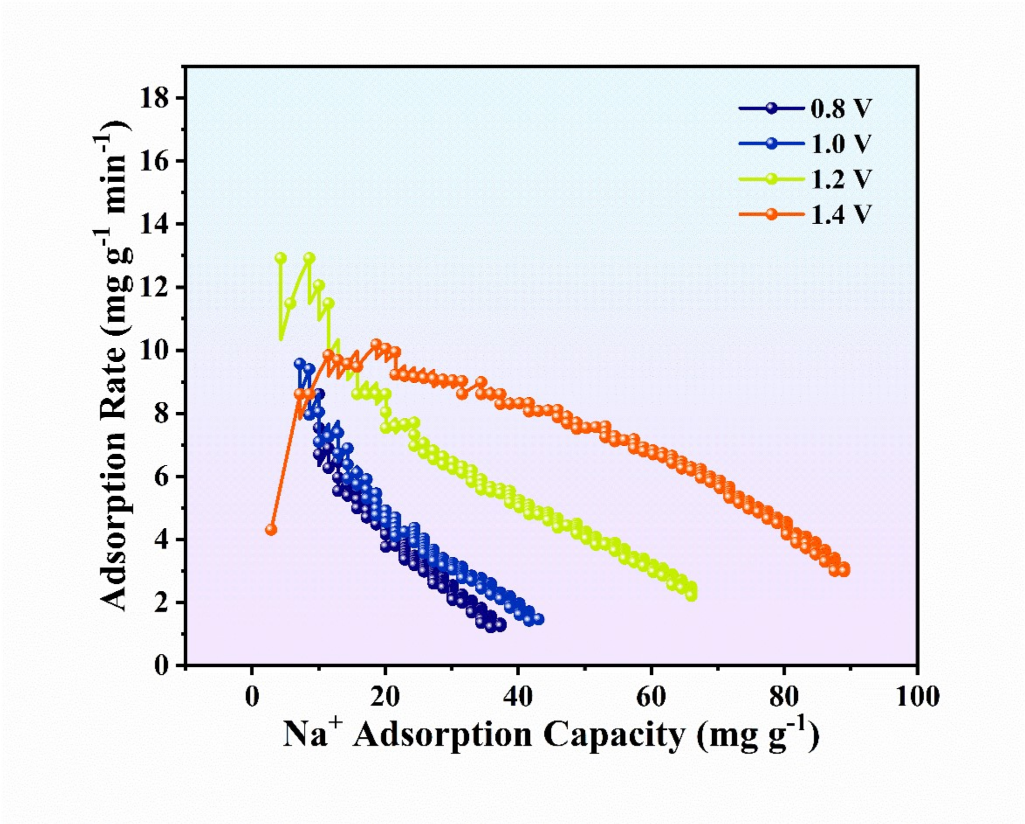

Fig S14. Na$^+$ Adsorption capacity and rate at different applied voltages

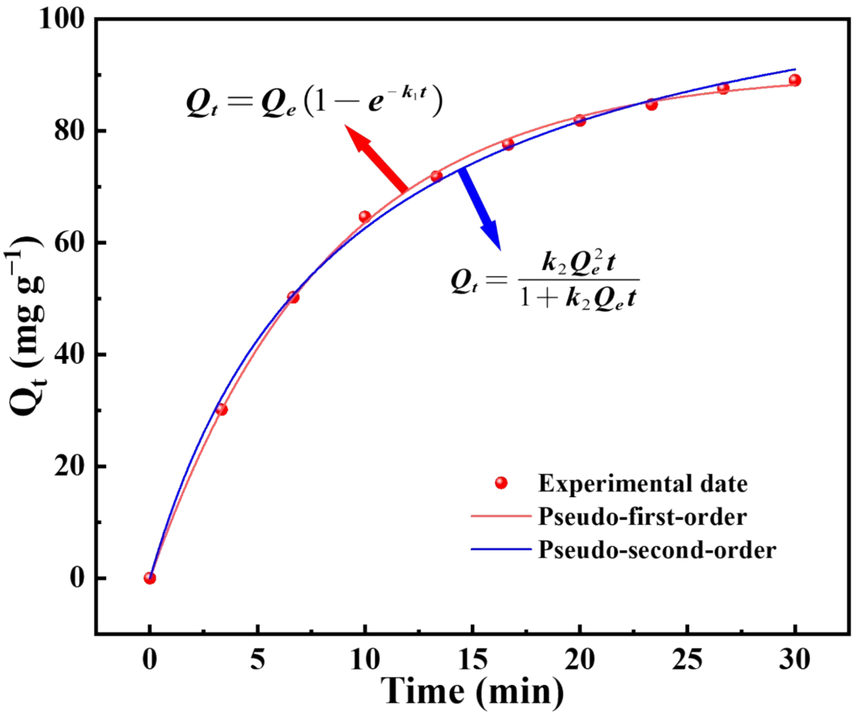

Figure S15. Pseudo-first-order and pseudo-second-order kinetic models for Na$^+$ removal by the assembled HCDI device at different times.

Table S3. The corresponding pseudo-first-order and pseudo-second-order kinetic parameters resulting from Figure S16.

Sample	**Pseudo-first-order**		**Pseudo-second-order**	
PIND	Q_e (mg g^{-1})	117.65	Q_e (mg g^{-1})	90.59
	k_1	9.65428e^{-4}	k_2	0.12097
	R^2	**0.9953**	**R^2**	**0.9989**

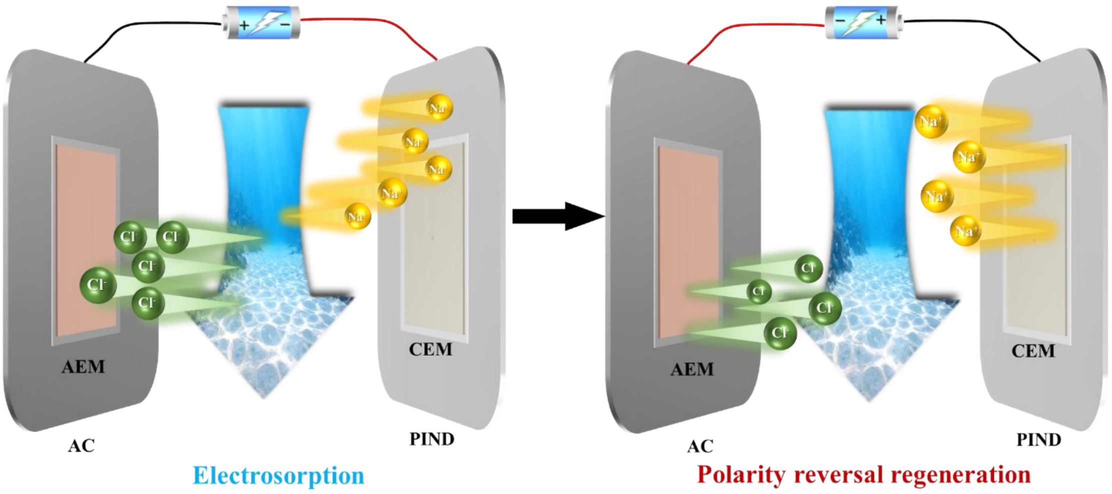

Figure S16. Schematic illustration of the two-stage operation of the PIND‖AC HCDI cell

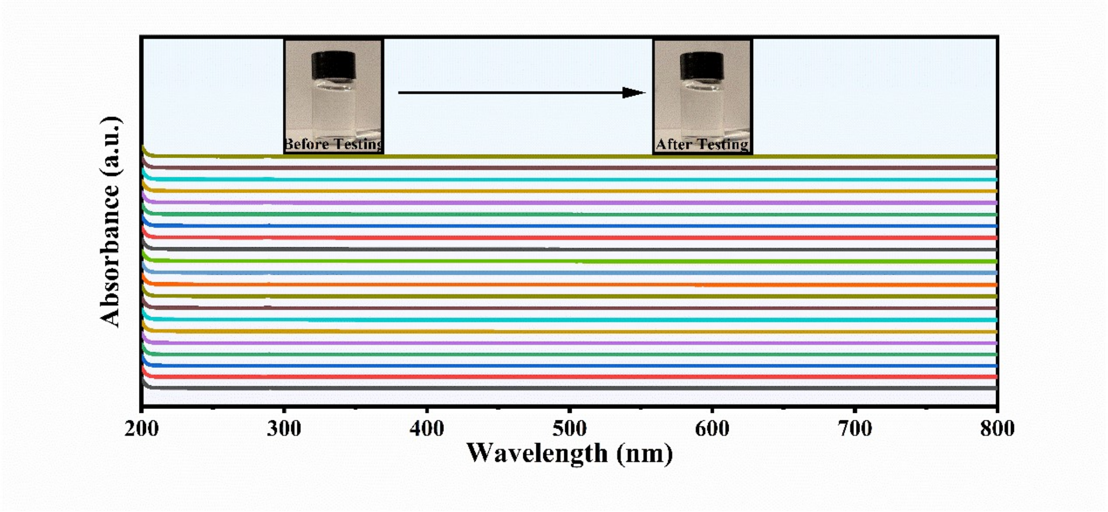

Figure S17. In situ UV-vis spectroscopy of electrolyte for PIND electrode during the charging-discharging process.

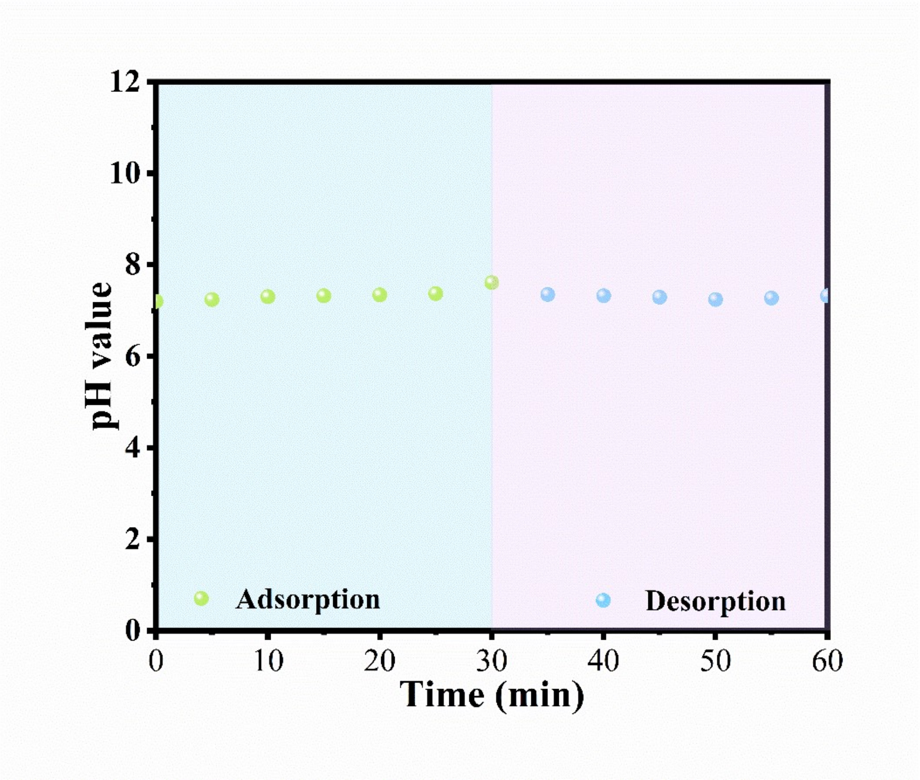

Figure S18. The pH curve corresponding to the adsorption/desorption process of HCDI system.

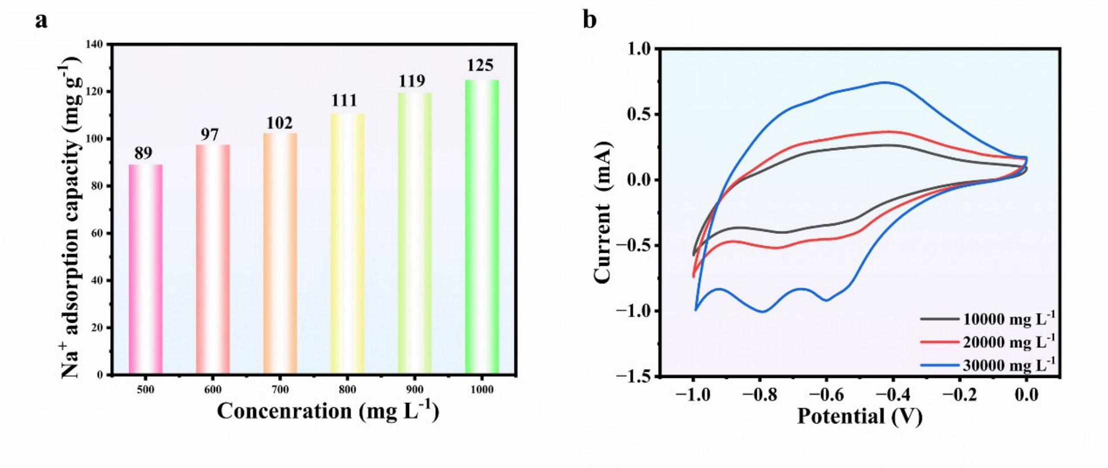

Figure S19. (a) Desalination capacity of HCDI system at different concentrations. (b) CV curves of PIND at different concentrations.